batteries

MDPI

Article

Cyclic Aging and Quasi-Static Indentation of Lithium-Ion Pouch Cells Under Maintained Spring-Loaded Confinement: Earlier Internal Short-Circuit Onset

Richard Polzer *, Vaishal Thirugnanam, Sergej Diel and Hans-Georg Schweiger

CARISSMA Institute of Electric, Connected and Secure Mobility (C-ECOS) , Technische Hochschule Ingolstadt, Esplanade 10, 85049 Ingolstadt, Germany; vaishal.thirugnanam@carissma.eu (V.T.)
* Correspondence: richard.polzer@thi.de

Abstract

Pouch cells in automotive modules age and may experience mechanical abuse while mechanically confined, yet almost all published comparisons of fresh and aged cells release the aging constraint before the abuse test. In the present work, three commercial 6 Ah pouch cells were electrochemically cycled to approximately 80% State of Health inside a spring-loaded flat-plate fixture initialized at a nominal average stack pressure of 0.11 MPa and were then indented quasi-statically at nominally 100% State of Charge without releasing the confinement. Three uncycled cells were tested as fresh references in the corresponding fixture configuration. The aging state was tracked by capacity fade and Electrochemical Impedance Spectroscopy. The aged cells built up force earlier, reaching 20 kN at 11% smaller intrusion, and the electrically detected Internal Short Circuit occurred at 18% lower displacement and at a 10% lower group-mean force, while peak force and displacement at peak remained within the observed cell-to-cell scatter. This differs from the right shift reported for many pouch-cell studies in which the aging constraint was released before testing and resembles the earlier onsets reported for hard-cased cylindrical cells. Following the electrically detected Internal Short Circuit onset, the aged-cell voltage reached 1 V later than that of the fresh references. The results are consistent with confinement history being a contributing and experimentally controllable variable in abuse tests on aged cells.

Keywords: lithium-ion batteries; pouch cell; stack pressure; preload; cyclic aging; mechanical abuse; indentation; internal short circuit; state of health; battery safety

Check for updates

Academic Editor: Changzhou Yuan

Received: 5 August 2026
Revised: 2 September 2026
Accepted: 9 September 2026
Published: 12 September 2026

Copyright: © 2026 by the authors. Licensee MDPI, Basel, Switzerland. This article is an open access article distributed under the terms and conditions of the Creative Commons Attribution (CC BY) license.

1. Introduction

Lithium-Ion Batteries (LIBs) are the dominant energy storage technology for electric vehicles because of their high energy and power density, long service life, and design flexibility [1]. As cells grow in size and energy content and are increasingly integrated into load-bearing vehicle structures, mechanical loads in crash scenarios pose critical risks to system safety [2]. Local intrusion can deform the layered electrode–separator assembly, rupture the separator, and trigger an Internal Short Circuit (ISC) that may escalate into Thermal Runaway (TR), fire, or explosion [3–5]. Indentation and crush tests are therefore firmly established as crash-relevant surrogate tests in research and regulation [6,7], and a substantial body of work has characterized the mechanical–electrical–thermal response of fresh cells as a function of indenter geometry [8,9], loading rate [10–12], State of Charge (SoC) [13,14], loading direction [15], and cell format [16]. This experimental baseline also underpins the mechanical cell models used in vehicle crash simulation [17–19].

Real battery packs, however, contain aged cells. Degradation mechanisms such as loss of lithium inventory, loss of active material, interphase growth, lithium plating, electrolyte depletion, gas generation, and irreversible electrode expansion alter the mechanical, electrical, and thermal state of a cell long before any abuse event occurs [20–24]. A growing number of studies have therefore compared the abuse response of fresh and aged cells. For pouch cells, most of these studies point in the same direction. Cells aged in the laboratory and indented without external constraint reach their characteristic markers at larger displacement than fresh cells. This rightward shift of the force–displacement response was reported for quasi-static indentation by Liu et al. [25], Kovachev et al. [26], Qu et al. [27], Jia et al. [28], and Guo et al. [29], for the pouch cells in the comparative study of Spettmann et al. [30], and for both the quasi-static and the dynamic tests of Sprenger et al. [31,32], while under high loading rates the first force peak of aged pouch cells remained almost unchanged [33]. Common explanations are compliant deposit layers on the electrode surfaces, gas pockets, and thickness growth that the indenter must first compress [25,27]. Notably, most of these cells were not aged free of load either. Liu et al. and Qu et al. aged their cells between screwed flat plates at an initial pressure of 0.05 MPa [25,27], Kovachev et al. at 0.06 MPa [26], and the cells of Sprenger et al. came from vehicle modules [31], but in all of these studies the constraint was released before the abuse test, whereas Jia et al. aged without preload [28,34]. The known exceptions with pouch cells are the large-format automotive cells studied by Gstrein et al. [35] and the field-aged cells with lithium plating examined by Abbas et al. [36], which failed earlier. Hard-cased cells behave differently: aged 18650 cells failed earlier or at unchanged thresholds [30,37,38], and for large-format tabless 4695 cylindrical cells our own previous work found a consistent leftward shift, with the displacement, force, and absorbed energy at ISC onset reduced by 16–38% after cycling to 80% State of Health (SoH) [39]. The aging path and the dominant aging mechanism additionally modulate these shifts [31,35,40–42]. In a recent survey of this literature, we found that no universal aging-driven shift emerges once the studies are normalized, and that the reported direction varies with cell format, aging pathway, and mechanical boundary conditions, particularly with whether the aging restraint is preserved during the subsequent abuse test [34].

One boundary condition regularly changes between service and test without receiving much attention, namely the stack preload. In automotive modules, pouch cells are compressed between rigid end plates, typically at initial pressures on the order of 0.1 MPa to 0.3 MPa, both to guarantee electrical and thermal contact and to control degradation [43,44]. The influence of this pressure on aging itself is well documented. Optimized compression extends cycle life and suppresses irreversible swelling [45,46], insufficient or inhomogeneous contact pressure accelerates local degradation [47], and the acting pressure influences interphase formation and lithium plating [48] as well as the strain state of the electrodes themselves [49]. The fixture concept (constant pressure versus fixed displacement) determines how the pressure evolves as the cell breathes and grows [50], and recent work demonstrates a direct interplay between stack pressure, mechanical expansion, and the dominant degradation pathway, with investigated pressures now reaching up to 1 MPa [51]. Preload also matters during abuse. External compression changes the crush response and the TR behavior of pouch cells [52], and simulation studies show that the preload force acting on a constrained pouch cell shifts the predicted short-circuit onset [53]. Reversible swelling couples the two aspects further, because the SoC-dependent thickness change of a constrained cell directly modulates the pressure acting at the moment of abuse [46].

Despite its relevance, stack preload is frequently discontinuous between aging and abuse-test protocols. Pouch cells may be aged under compression but are commonly removed from the fixture before mechanical testing. In our recent review, we termed

this discontinuity a lack of confinement continuity [34]. Releasing the aging restraint changes the mechanical starting state of the pouch cell and may therefore contribute to the different aging-induced shifts reported across studies. Hard-cased cylindrical and prismatic cells, by contrast, retain their casing-imposed constraint throughout both service and testing. Abuse tests that keep a pouch cell mechanically confined during the test are themselves rare. Höschele et al. indented fresh pouch cells inside a preload fixture and used this configuration to examine reversible swelling and preload force in short-circuit prediction [46]. To the best of the authors' knowledge, however, no published study has combined cyclic aging of pouch cells under a defined stack preload with subsequent indentation in the same mounted fixture, so that the confinement remains continuous from the first cycle to the abuse test.

The present study provides an initial experimental investigation of this condition. Commercial 6 Ah pouch cells were mounted in a flat-plate fixture initialized at a nominal average stack pressure of 0.11 MPa, electrochemically cycled to approximately 80% SoH, and subsequently indented quasi-statically at 100% SoC without removing the fixture. Uncycled cells from the same batch were tested as fresh references using the corresponding fixture configuration and the same nominal initial preload. The comparison therefore contrasts fresh cells with cells whose mechanical boundary condition was preserved throughout aging and abuse testing. The aging state was tracked by capacity fade and Electrochemical Impedance Spectroscopy (EIS), while the abuse response was characterized by synchronized force, displacement, and voltage measurements.

The study examines whether the rightward shift reported for aged pouch cells tested after removal of the aging restraint also occurs under confinement continuity [25–27,30,31]. We hypothesized that the aged cells would instead build up force earlier and reach the electrically detected ISC onset at smaller intrusion than the fresh references, consistent with observations for hard-cased cells [34,39]. The study additionally provides a fresh-to-aged dataset obtained with a common fixture architecture and outlines a test matrix for the broader investigation of preload history in mechanical abuse testing.

2. Materials and Methods

2.1. Test Cells

Commercial Lithium-Ion polymer pouch cells of type FE906090 (Fullest Energy Co., Ltd., Shenzhen, China) were used for all experiments. The product-specific data sheet specifies a nominal capacity of 6.0 Ah, a nominal voltage of 3.7 V, and nominal dimensions of 90 × 60 × 9 mm (length × width × thickness), corresponding to a large-face footprint of approximately 54 cm^2. A safety data sheet issued for the manufacturer's Lithium-Ion pouch cells specifies lithium cobalt oxide ($LiCoO_2$) and graphite as the principal electrode materials. Six cells purchased in the same order were used. Three cells were assigned to the aged group (cells 03, 04, and 05) and three served as uncycled fresh references (cells 01, 02, and 06). The fresh cells were stored at room temperature for the duration of the aging campaign and tested in the as-received state, so that both groups had the same calendar age at the time of the abuse tests. The measured initial discharge capacities of the aged-group cells were between 5.74 Ah and 6.02 Ah.

2.2. Preload Fixture

The core of the experimental concept is a spring-loaded flat-plate fixture that maintains mechanical confinement during both cyclic aging and the final abuse test (Figure 1). The pouch cell is positioned between two rigid steel plates, each measuring 140 × 110 × 10 mm. Four compression springs with a spring rate of 35.16 N mm^{-1} each are guided on threaded rods at the plate corners and press the upper plate onto the cell. The springs act mechani-

cally in parallel, giving a total nominal fixture stiffness of 140.64 N mm^{-1}. The upper plate contains a central opening with a guided, flat-ended indenter. During aging, the lower face of the indenter was flush with the lower face of the upper plate. A shoulder on the indenter was seated directly against the upper plate under the spring load, so both components acted as one continuous planar loading surface. During the abuse test, the actuator pushed the indenter shoulder from this seat and displaced the indenter relative to the upper plate to introduce the local intrusion, following the boundary-condition concept used by Höschele et al. [46].

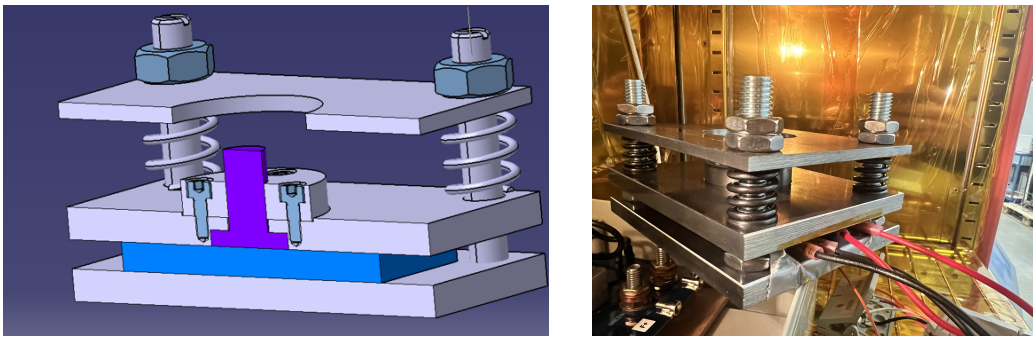

(**a**) (**b**)

Figure 1. Preload fixture. (**a**) Sectioned CAD view. The 90 × 60 × 9 mm pouch cell (blue) is positioned between two steel plates and compressed by four guided springs. During aging, the lower face of the indenter (purple) is flush with the lower face of the upper plate. (**b**) Fixture with an installed cell during cyclic aging in the climate chamber.

The preload was set by tightening each nut by 2.5 turns from the snug position. With the 1.5 mm thread pitch, this corresponds to an additional axial nut travel of 3.75 mm. Because the snug position already included initial spring contact, the thread travel served as the repeatable setting procedure, whereas the preload force was calculated from the total spring compression relative to the unloaded spring length measured with a dial gauge at one corner of the plates. The summed initial preload force was approximately 0.6 kN, corresponding to an average spring compression of approximately 4.27 mm, and to a nominal average pressure of 0.11 MPa over the 90 × 60 mm pouch-body footprint. This value lies in the range of initial compressions reported for automotive pouch-cell stacks [43,44] and at the lower end of the pressure range examined in recent stack-pressure studies [45,51].

The springs were selected to provide a substantially more compliant boundary condition than directly bolted fixed-displacement plates. For an idealized increase in cell thickness Δh, the spring force changes according to $\Delta F = k_{\Sigma} \Delta h$. As an order-of-magnitude reference, Aufschläger et al. reported approximately 1.8 % reversible swelling at beginning of life, approximately 1.0 % to 1.2 % reversible swelling at end of life, and up to 3.4 % irreversible swelling for flexibly compressed NMC622/graphite pouch cells [45]. Applied to the nominal 9 mm thickness of the present cells, 1.8 % cycle-scale swelling would increase the idealized fixture force by approximately 23 N (3.8 %). A literature-based end-of-life combination of 3.4 % irreversible and approximately 1 % reversible swelling would correspond to approximately 0.40 mm thickness increase, 56 N additional spring force, and a nominal average pressure of approximately 0.121 MPa. These calculations are sensitivity estimates, because the cell-thickness evolution, seating and relaxation of the assembly, and spatial pressure redistribution were not measured [50,51].

Each aged cell remained mounted in one of three nominally identical fixtures, with unchanged nut positions, from the first cycle to the end of its abuse test. The fixtures were subsequently reused for the fresh-reference tests. Post-test inspection revealed no visible plastic deformation of the plates or springs, and the nominal initial preload was re-

established using the same procedure before each fresh-cell test. Both groups were therefore tested with the same fixture architecture and nominal initial preload, while differing in their electrochemical aging and in the months of mechanical conditioning under confinement experienced by the aged cells.

2.3. Cyclic Aging and Capacity Checks

The three aged-group cells were cycled on a NEWARE CT-4008-5V6A-A battery test system inside an ACS DY200 climate chamber (ATT ATT Umweltsimulation GmbH, Ofterdingen, Germany) at 22 °C while mounted in the preload fixture. Cycling was performed in blocks of 100 full-depth cycles between 2.8 V and 4.2 V, corresponding nominally to 100 % depth of discharge (DoD) between 0 % and 100 % SoC. Each cycle comprised a 1C constant-current–constant-voltage (CC-CV) charge to 4.2 V, with the CV phase terminated at 0.5 A, followed by a 1C constant-current discharge to 2.8 V. After every block, a reference-capacity check was performed over the same voltage window using a 0.5C CC-CV charge and a 0.5C constant-current discharge, with the CV phase terminated at 0.3 A. Each capacity check comprised two complete discharges, whose capacities were averaged.

Aging was stopped when the 0.5C reference capacity approached 80% of its initial value, which required 530, 550, and 600 cycles for cells 03, 04, and 05. The final capacity retentions were 81.1 %, 81.8 %, and 82.3 % (mean $81.7 \pm 0.6\%$), so the aged group is denoted SoH 80 in the following. After the final cycling block and reference-capacity check, the cells remained mounted in their fixtures during storage until the abuse tests.

2.4. Electrochemical Impedance Spectroscopy

EIS was measured on each aged-group cell in the fresh state before cycling and again after the final cycling block, in both cases at 100% SoC and 25 °C following a rest period of 24 h after charging. Galvanostatic spectra were recorded from 10 kHz to 10 mHz with an excitation amplitude of 100 mA using a ZAHNER Zennium IM6 (Zahner-Elektrik GmbH & Co. KG, Kronach, Germany). The measured spectra were compared directly in the Nyquist representation. For direct quantitative comparison, the real impedance at 10 kHz was evaluated. The 10 mHz endpoint and the measured span between 10 mHz and 10 kHz are retained in the Supplementary Material as descriptive values. The low-frequency endpoint was not used for process-specific interpretation because the spectra do not close at the lower-frequency boundary. In addition, an equivalent circuit consisting of a series inductance L, a series resistance R_0, and one depressed arc, represented by a resistance R_{arc} in parallel with a constant-phase element of exponent n, was fitted to each spectrum by complex non-linear least squares with modulus weighting. The fit was restricted to the frequency window containing the arc, that is from the local minimum of $-Z''$ that marks the onset of the low-frequency branch up to the highest frequency at which $-Z''$ is still positive. Fit quality is reported as the relative root-mean-square residual of the weighted residuals and as the absolute root-mean-square residual. Data consistency was checked beforehand with a linear Kramers–Kronig-compliant fit [54]. The complete fit diagnostics, including the parameter profiles, the identifiability tests and the Kramers–Kronig residuals, are provided in the Supplementary Material.

2.5. Abuse Test

For the abuse tests, the preload fixture was mounted on a dedicated test stand (Figure 2). All six cells were tested at ambient temperature of approximately 25 °C and nominally 100% SoC. They were charged at 0.5C in CC-CV mode to 4.2 V with a 0.3 A cut-off current, following the same protocol as the capacity checks, and rested for 24 h before the test. The open-circuit voltages at test start were between 4.06 V and 4.07 V. Three nominally identical fixtures were used, each first for one aged cell and subsequently for one fresh ref-

erence as described in Section 2.2. The movable indenter of the fixture, a flat-ended cylinder with a diameter of 20 mm, was pressed into the large face of the cell through the opening of the upper plate. The average measured displacement rate during loading was 0.125 mm s^{-1}, and loading continued until the force maximum had been passed. The force was measured with four KD80s 20 kN load cells (ME-Meßsysteme GmbH, Hennigsdorf, Germany), whose sum is reported as the indentation force. The indenter displacement was measured with an FHTA19-020025 LVDT position sensor (ABEK Sensoren, Tönisvorst, Germany) locally between the indenter-side upper plate and the lower plate carrying the cell. This arrangement minimizes contributions from machine and external frame compliance. The force, displacement, and voltage signals were recorded synchronously. Electrical event detection and time-based voltage metrics were evaluated with an effective temporal resolution of 0.10 s. The mechanical evaluation window extended from the start of the test to a post-peak decay of the force to 55 % of its maximum. All mechanical characteristic values reported here lie at or before the force maximum and are therefore independent of this bound. The voltage was acquired and evaluated beyond the window, so the time from the ISC onset to 1 V is unaffected by it. The response after the ISC was evaluated from the cell voltage, the test recordings, and the post-test condition of the cells. All tests were video-recorded for documentation. The recordings were reviewed after the experiments to determine whether visible gas or aerosol emission occurred. This assessment was qualitative and was not used to infer gas composition, TR, or thermal severity. Exploratory thermocouples were positioned adjacent to the cells without controlled cell–surface contact. Their signals were used only for experimental monitoring and were not evaluated quantitatively.

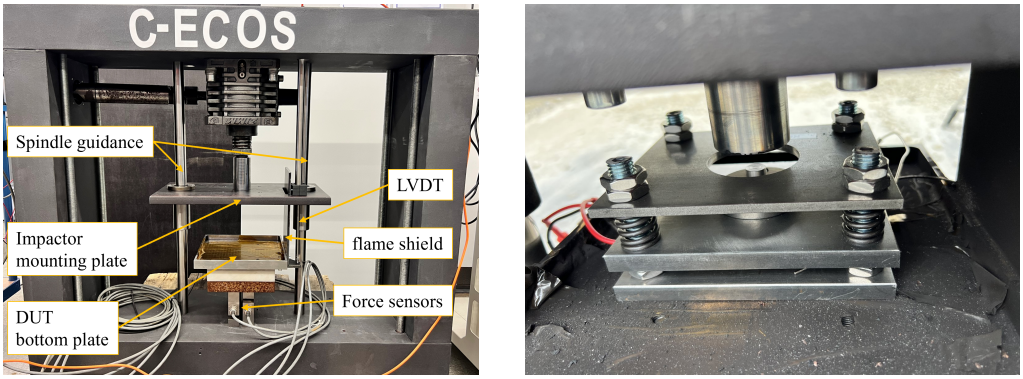

Figure 2. Abuse test setup. (**a**) Test stand. (**b**) Close-up of the fixture immediately before the test.

2.6. Evaluation of the Measured Signals

Data processing followed the procedure of our previous work [39]. Force signals were median-filtered over seven samples, smoothed with a second-order Savitzky–Golay filter using a 0.4 s window, and resampled on a common displacement grid with a spacing of 2.5 µm. The displacement was referenced to the relative plate position at test start, with the preload applied. No horizontal alignment of the individual curves was performed.

The out-of-plane indentation of a pouch cell produces a force–displacement curve with a characteristic shape (Figure 3a). An initially compliant toe region, in which pouch slack and surface unevenness are flattened, is followed by progressive stiffening as the porous coatings densify. The curve then flattens, because layers inside the electrode stack begin to crack and lose load-bearing capacity, and the force finally passes through a maximum when the stack collapses structurally [8,27]. The stiffening of the pre-peak regime is quantified by the displacement $\delta(F_{\mathrm{ref}})$ required to reach fixed reference forces of 10, 20, and 30 kN, which captures the position of the whole loading branch without relying on a derivative. The structural collapse is characterized by the peak force F_{max} and the displacement at

peak force δ_{peak}. The ISC onset (F_{ISC}, δ_{ISC}) is detected electrically, because the macroscopic force–displacement response alone does not uniquely indicate when internal electrical contact is established. Both absolute and relative voltage criteria are in use for this purpose. Lamb and Orendorff declare the event at an absolute drop of 100 mV and note explicitly that a different threshold would shift the declared onset [55], whereas other studies apply relative rules tied to a floating average of the voltage over the preceding intrusion interval [11].

The pre-test baseline was defined as the median voltage over the first 1.0 s of the recording. The ISC onset was then defined as the first drop by at least 100 mV below this baseline that persisted for at least 0.10 s (Figure 3b). This definition follows the absolute-threshold practice of [55]. Criterion robustness was assessed by repeating the detection for drops of 50, 100, and 200 mV while retaining the same persistence criterion. The per-cell sensitivity results are provided with the Supplementary Material.

In addition, the external mechanical work up to peak force, $W_{peak} = \int_0^{\delta_{peak}} F(\delta)\,\mathrm{d}\delta$, was calculated from the processed force–displacement curve. The time from ISC onset to a cell voltage of 1 V was evaluated as a secondary descriptor of the electrical collapse. The 1 V threshold lies far below the operating window and marks near-complete voltage decay through the short-circuit path.

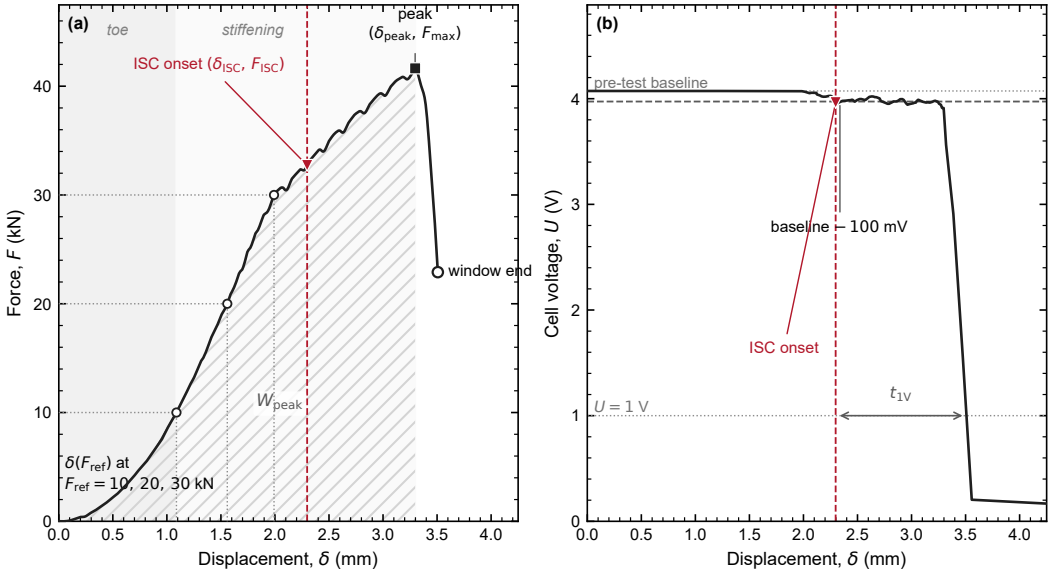

Figure 3. Definition of the evaluated characteristic values, shown on cell 01. (**a**) Force–displacement curve with the compliant toe region, the stiffening regime, the displacements $\delta(F_{ref})$ at which the reference forces of 10, 20, and 30 kN are reached, the external mechanical work W_{peak} as the hatched area up to the peak, the peak point, the electrically detected ISC onset, and the end of the mechanical evaluation window. (**b**) Cell voltage with the pre-test baseline, the 100 mV detection criterion, and the interval to a cell voltage of 1 V. The dashed red line marks the ISC onset in both panels.

All group results are reported as mean ± one standard deviation of the three cells per group. Given the small sample size, the statistical analyses are treated as descriptive. The individual values are shown alongside the group statistics in all figures, and group differences are interpreted conservatively in the light of the observed cell-to-cell spread (Section 4.3). No confirmatory hypothesis test is used as the basis for any conclusion, and no claim of statistical significance is made. Table 1 reports for each characteristic value the observed range of the three individual cells and the standardized mean difference expressed as Hedges' g, that is Cohen's d with the small-sample bias correction $J = 1 - 3/(4\nu - 1)$ applied [56,57], together with its 95% confidence interval obtained from the noncentral t distribution. The values were computed from the individual cell measurements. Ex-

ploratory two-sided Welch unequal-variance t-tests with continuous Welch–Satterthwaite degrees of freedom are provided in the Supplementary Material. They are reported for transparency and are not used to support any conclusion, because the sample size, the correlated nature of the descriptors, and the absence of pre-specified hypotheses preclude confirmatory inference.

Table 1. Characteristic values of the abuse tests (mean ± standard deviation, $n = 3$ per group). Square brackets in the group columns give the observed range of the three individual cells. The rightmost column reports the bias-corrected standardized mean difference (Hedges' g) with its 95% confidence interval, computed from the unrounded individual-cell values as a descriptive characterization of the group separation and not as a significance test (Section 2.6). Exploratory Welch t-tests are provided in the Supplementary Material.

Quantity	Fresh	Aged (SoH 80)	Change	Hedges' g [95% CI]
Loading and trigger descriptors				
Displacement to 10 kN, $\delta(F_{10})$ (mm)	0.97 ± 0.11 [0.87–1.09]	0.80 ± 0.04 [0.75–0.83]	−18%	1.65 [−0.09, 3.28]
Displacement to 20 kN, $\delta(F_{20})$ (mm)	1.44 ± 0.12 [1.33–1.56]	1.28 ± 0.04 [1.24–1.32]	−11%	1.48 [−0.19, 3.04]
Displacement to 30 kN, $\delta(F_{30})$ (mm)	1.86 ± 0.13 [1.74–1.99]	1.75 ± 0.06 [1.68–1.81]	−6%	0.90 [−0.56, 2.27]
ISC displacement δ_{ISC} (mm)	2.24 ± 0.17 [2.06–2.38]	1.84 ± 0.19 [1.61–1.95]	−18%	1.80 [−0.01, 3.51]
ISC force F_{ISC} (kN)	34.5 ± 1.9 [32.7–36.6]	30.9 ± 3.3 [27.2–33.5]	−10%	1.08 [−0.44, 2.50]
Global collapse descriptors				
Peak force F_{max} (kN)	40.7 ± 3.2 [37.1–43.2]	38.2 ± 1.8 [36.5–40.1]	−6%	0.75 [−0.66, 2.09]
Displacement at peak force δ_{peak} (mm)	2.95 ± 0.47 [2.41–3.30]	3.03 ± 0.11 [2.97–3.16]	+3%	−0.20 [−1.48, 1.10]
External mechanical work up to peak force W_{peak} (J)	60.3 ± 17.9 [39.8–72.6]	66.5 ± 3.9 [62.2–70.0]	+10%	−0.38 [−1.66, 0.95]
Post-trigger electrical descriptor				
Time from ISC to 1 V (s)	5.2 ± 3.4 [1.3–7.3]	9.8 ± 1.9 [8.7–12.0]	+88%	−1.34 [−2.85, 0.27]

3. Results

3.1. Capacity Fade

Figure 4 shows the 0.5C reference-capacity checks used to determine SoH. The capacity decreased smoothly for all three cells and reached 81.7 ± 0.6% of the initial value after 530 to 600 cycles, at which point cycling was stopped. Moderate stack pressure has been reported to promote uniform degradation in pouch cells [43,45], although the present data do not allow this to be verified for the fixture used here.

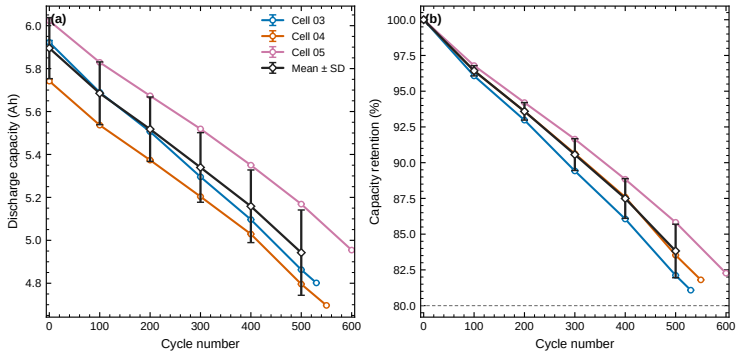

Figure 4. The 0.5C reference-capacity checks after each aging block and at the final state. Discharge capacity (**a**) and capacity retention relative to the initial check (**b**) for the three aged-group cells. These measurements define the reported SoH. The black Mean ± SD trace is shown only at cycle counts reached by at least two of the three cells. The three cells were stopped individually at 530, 550, and 600 cycles, so beyond 500 cycles only the per-cell traces are shown.

3.2. Impedance Evolution

Figure 5 summarizes the impedance evolution of the aging-group cells from their Beginning of Life (BoL) state to the aged state at 100% SoC. The measured Nyquist spectra shifted towards higher real impedance and the depressed arc widened after aging in all

three cells. Read directly from the spectra, the real part of the impedance at 10 kHz increased from 28.8 ± 0.1 to 38.1 ± 1.7 mΩ (+32%). The consistent impedance increase across all three cells provides an independent characterization of the aged state. This reading is model-free: at the highest measured frequency the depressed arc still contributes to the real part, so the value lies above the series resistance R_0 obtained from the equivalent-circuit fit below. The two-electrode spectra do not permit a unique assignment of the changes to individual electrodes or degradation mechanisms.

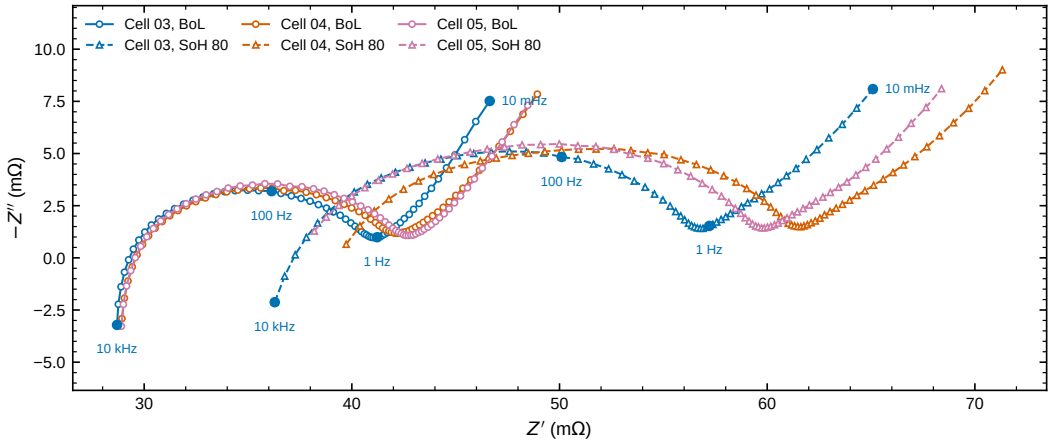

Figure 5. Nyquist spectra of the three aging-group cells in the BoL state (0 cycles) and after aging to SoH 80 (530–600 cycles), measured at 100% SoC. Colors distinguish cells 03–05; solid lines with circles denote BoL, and dashed lines with squares denote SoH 80.

To resolve this increase into a series and a polarization contribution, the equivalent circuit $L + R_0 + (R_{\mathrm{arc}} \| Q)$ was fitted to each spectrum over the frequency window containing the arc (Section 2.4). Figure 6a shows an enlarged view of this region and the corresponding fits. The model reproduced all six spectra with relative residuals of 0.16 % to 0.37 %, corresponding to absolute residuals of 0.09 mΩ to 0.28 mΩ. Aging increased the series resistance R_0 from 27.64 ± 0.04 to 34.81 ± 0.38 mΩ, by 25 to 27% in the individual cells (Figure 6b), and the arc resistance R_{arc} from 15.21 ± 0.88 to 26.28 ± 2.32 mΩ, by 67 to 83% (Figure 6c). The impedance increase is thus carried mainly by the polarization arc rather than by the series resistance. The constant-phase exponent was 0.46 to 0.55 in all six fits, that is the arc is depressed and its response is distributed over a broad range of relaxation times.

Whether this arc can be subdivided further, as would be required to separate interphase-related and charge-transfer-related contributions, was tested using a two-element model. For both the BoL and aged spectra, the individual contributions remained weakly constrained, and the data therefore do not support a unique separation of these processes. The spectra are consequently evaluated in terms of R_0 and R_{arc} only. Full identifiability diagnostics are provided in the Supplementary Material.

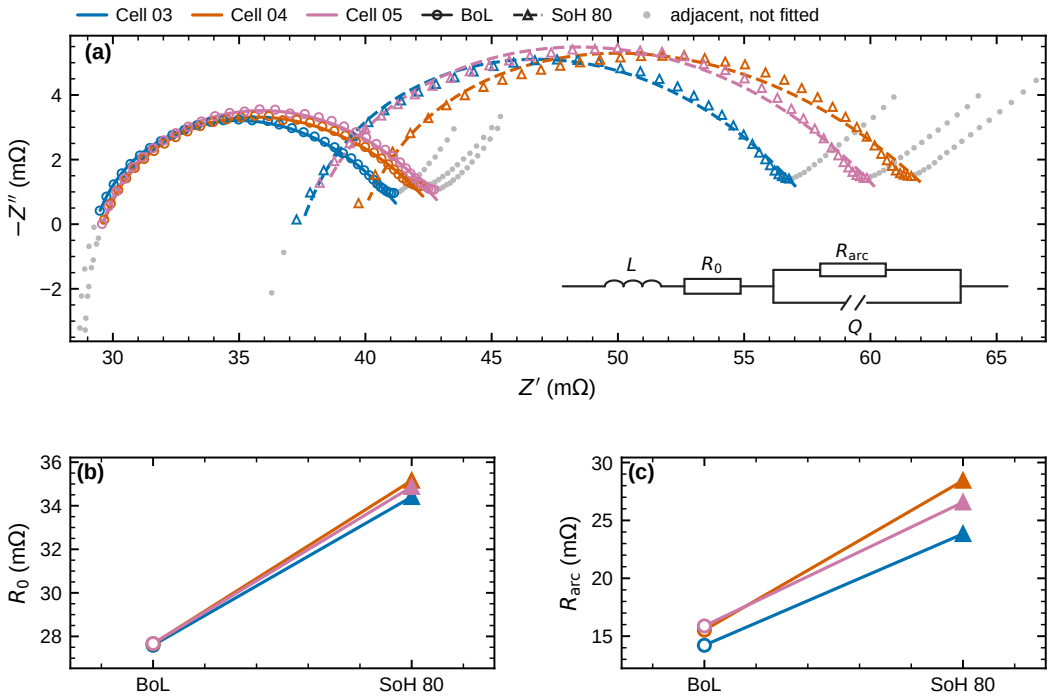

Figure 6. Equivalent-circuit analysis of the aging-group spectra. (**a**) Enlarged view of the retained arc region, showing the measured spectra (symbols) and $L + R_0 + (R_{arc}\|Q)$ fits (lines), with the circuit shown as an inset. Grey dots mark the adjacent measured points outside the fitted window, which were not modelled. (**b**) Series resistance R_0 and (**c**) arc resistance R_{arc} for each cell in the BoL and aged state. Marker shape encodes the state in addition to color: open circles denote BoL, filled triangles the aged (SoH 80) state.

3.3. Mechanical Response

Figure 7a compares the force–displacement curves of all six cells, indented using the same fixture architecture and nominal initial preload. All curves show the response described in Section 2.6, with a compliant toe region, densification-driven stiffening, and a force maximum followed by structural collapse. The three aged curves rise earlier and lie above the fresh-group mean over most of the pre-peak loading branch. With the aging fixture left mounted, aging shifted the pre-peak force build-up and, as shown below, the ISC onset to smaller displacement, which is referred to as a left shift in the following. Comparable pouch cells aged under compression but tested after release from the aging constraint showed a rightward shift [25–27,31]. Individual ranges partially overlap near 30 kN and toward peak force, but the group-mean displacement remains smaller at all three reference forces and at ISC onset.

The characteristic values (Figure 8 and Table 1) quantify the shift. Because the aged cells build up force earlier, they reach every reference load at a smaller intrusion. The displacement to reach 10 kN decreased from 0.97 ± 0.11 to 0.80 ± 0.04 mm (−18%), the displacement to reach 20 kN from 1.44 ± 0.12 to 1.28 ± 0.04 mm (−11%), and the displacement to reach 30 kN from 1.86 ± 0.13 to 1.75 ± 0.06 mm (−6%). The shift is thus largest early in the loading branch and diminishes toward the peak. The global collapse quantities changed much less: the peak force decreased by only 6% (from 40.7 ± 3.2 to 38.2 ± 1.8 kN), while the displacement at peak force changed by 3%. The group-mean external mechanical work up to peak force was 10% higher for the aged cells (66.5 ± 3.9 versus 60.3 ± 17.9 J), but the individual ranges overlapped and the difference does not indicate a clear group-level shift at $n = 3$. Under the tested boundary condition, aging mainly advances the force build-up and the onset of electrically detectable short-circuiting, whereas the global peak and work-to-peak descriptors remain comparatively similar.

The origin of the shift becomes clearer when displacement increments are considered instead of absolute values. The displacement increment from 10 to 20 kN was 0.47 ± 0.01 mm for the fresh cells and 0.48 ± 0.03 mm for the aged cells. From 20 to 30 kN, it was 0.42 ± 0.01 and 0.47 ± 0.02 mm, respectively. The compressed-stack response between 10 and 30 kN therefore does not indicate greater secant stiffness of the aged cells over these intervals, and the largest group separation occurs in the early loading branch. The remaining intrusion from 10 kN to the ISC onset was 1.27 ± 0.14 mm for the fresh cells and 1.04 ± 0.21 mm for the aged cells, a reduction of 19%. At the group level, most of the additional separation accumulated between the 30 kN reference position and ISC onset; cell 03 was an exception because its ISC criterion was reached before the force attained 30 kN. This is the central observation of the present comparison: a purely horizontal offset of the loading curve, such as a difference in initial seating, would displace all reference-force positions equally and leave the interval from 10 kN to the ISC onset unchanged. The earlier ISC is therefore not explained solely by the offset of the initial toe region.

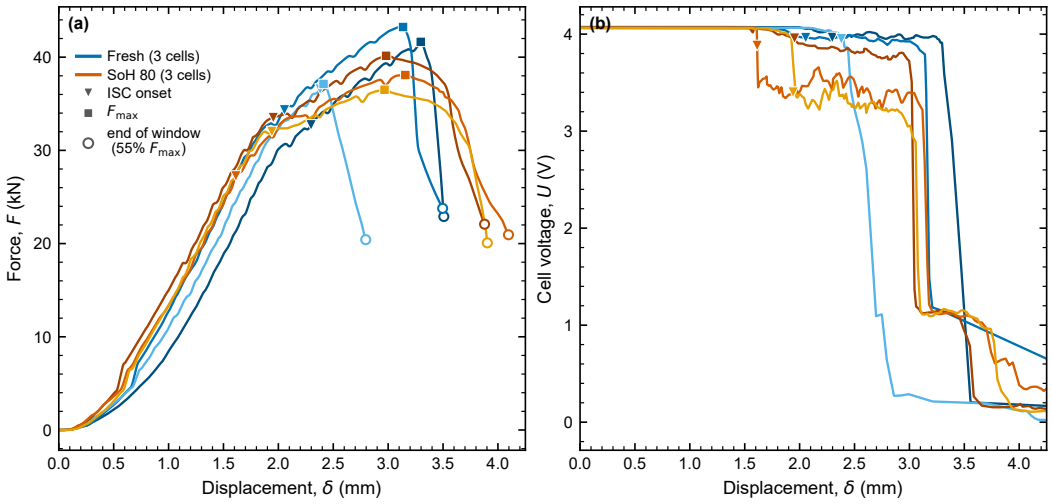

Figure 7. Mechanical and electrical response, both panels sharing the same displacement axis. (**a**) Force–displacement curves of all six cells over the mechanical evaluation window. Squares mark the force maximum, open circles the end of the window at 55 % of the individual peak force, and triangles the ISC onset. (**b**) The corresponding cell voltage, acquired beyond the mechanical window. Blue shades denote the three fresh cells and orange shades the three aged cells.

Across most mechanical descriptors—particularly the reference-force positions, peak quantities, and work to peak—the aged group shows lower cell-to-cell scatter than the fresh group; ISC displacement and ISC force are exceptions. For example, the displacement to reach 20 kN scatters with a coefficient of variation of 3% for the aged cells against 8% for the fresh cells, and the mechanical work to peak with 6% against 30%. The reduction is most pronounced in the early loading region, where the standard deviation of the displacement to 10 kN drops from 0.11 to 0.04 mm, while the subsequent displacement increments scatter similarly in both groups. Much of the fresh-group spread in the collapse-related descriptors originates from cell 06, which reached its force maximum at the smallest displacement and gave the lowest work to peak of all six tests. A leave-one-out sensitivity analysis shows that excluding this cell markedly reduced the scatter of the collapse-related descriptors. Excluding cell 06 lowers the fresh-group coefficient of variation from 16% to 4% for the peak displacement, from 30% to 4% for the work to peak, and from 7.8% to 2.7% for the peak force. For the displacement to 10, 20, and 30 kN, excluding cell 06 changes the coefficient of variation from 11% to 16%, from 8% to 11%, and from 7% to 10%, respectively, because its values lie near the center of the three fresh-cell values in the pre-peak region. Peak force, peak displacement, and work to peak are all linked to the same collapse event and therefore

describe one specific feature of the force–displacement curve of this cell. All individual values are shown in Figure 8. This comparison therefore remains a descriptive observation. A plausible explanation is that the aged cells enter the test in a consolidated state after months under pressure, whereas as-received cells differ in internal gaps, winding tension, and surface waviness.

The observed group ranges do not overlap for the displacements to 10 and 20 kN or for the ISC displacement, whereas they overlap for the displacement to 30 kN, the ISC force, and the global collapse descriptors. The earlier shift is therefore consistent for selected loading and trigger descriptors within the six tested cells, but is not uniform across all mechanical descriptors.

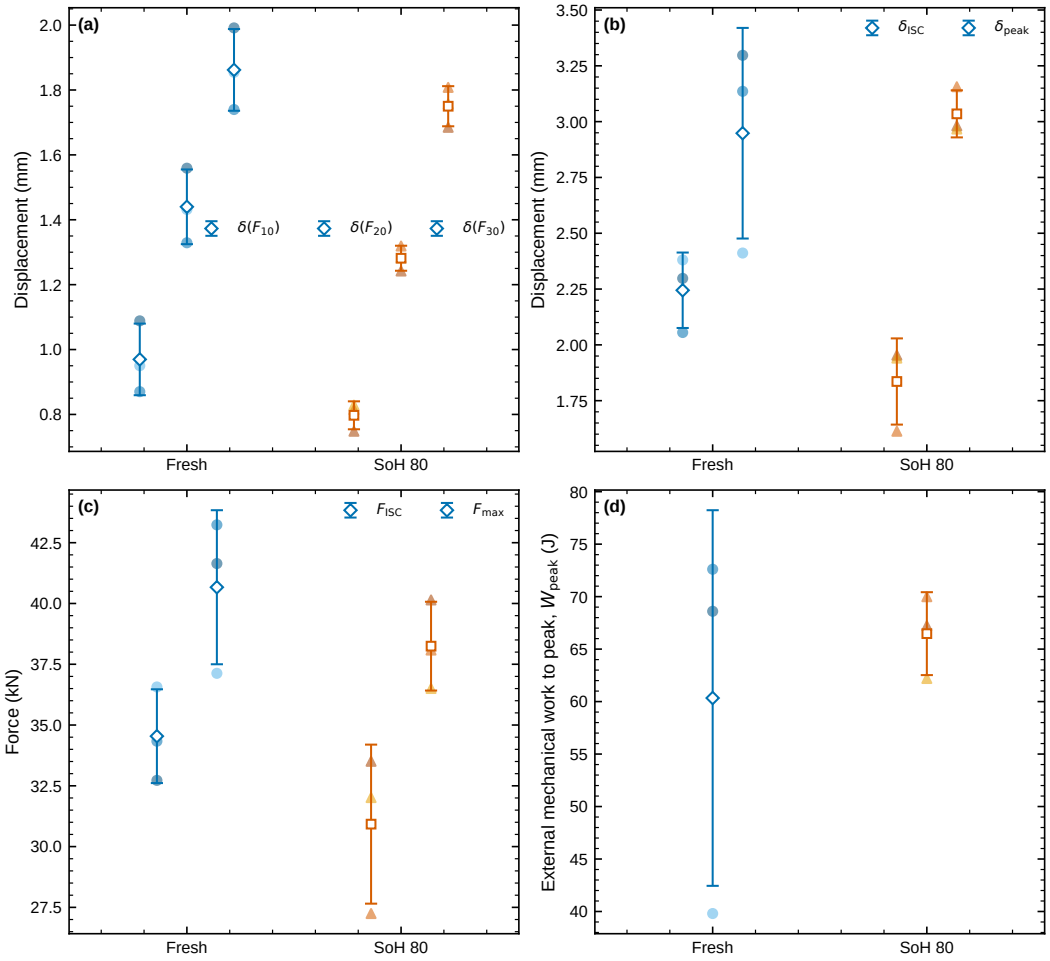

Figure 8. Characteristic values of the abuse tests. (**a**) Displacement to reach the reference forces of 10, 20, and 30 kN. (**b**) Displacement at the ISC onset and at peak force. (**c**) Force at the ISC onset and at the peak. (**d**) External mechanical work up to peak force. Open symbols show the group mean with standard deviation and filled symbols the individual cells. Marker shape encodes the group in addition to color: circles and open diamonds denote fresh cells, triangles and open squares denote the aged (SoH 80) cells.

3.4. Electrical Response and Post-Test Condition

All six tests produced an electrically detected ISC before the force maximum. Consistent with the mechanical left shift, the aged-group mean ISC onset occurred at 18% smaller displacement (1.84 ± 0.19 versus 2.24 ± 0.17 mm) and at a 10% lower force (30.9 ± 3.3 versus 34.5 ± 1.9 kN), as visible directly in the two panels of Figure 7. The direction of this difference was preserved for voltage-drop thresholds of 50, 100, and 200 mV: depending on the threshold, the aged-group onset occurred at 18.2–35.2% smaller mean displacement and

10.2–22.4% lower mean force. The larger separation at 200 mV resulted from this threshold identifying a later stage of the voltage decrease in two fresh cells. Following the ISC onset, the time to reach 1 V increased from 5.2 ± 3.4 to 9.8 ± 1.9 s (Figure 9). This metric is treated as a secondary descriptor of the electrical decay because the short-path resistance and current were not measured and the groups contained different absolute stored charge at the same nominal SoC. Review of the test recordings showed visible gas or aerosol emission in all three fresh-cell tests and in one of the three aged-cell tests (Table 2). This qualitative observation is not interpreted as a measure of thermal severity. As an example, Figure 10 shows the post-test condition of the aged cell for which visible emission was observed. The comparison of the post-trigger behavior therefore rests on the electrical signals and these qualitative observations.

Table 2. Qualitative visual observations from the test recordings. The classification is binary and does not imply a specific gas composition or thermal severity.

Cell	Group	Visible Gas/Aerosol Emission
Cell 01	Fresh	yes
Cell 02	Fresh	yes
Cell 06	Fresh	yes
Cell 05	SoH 80	no
Cell 03	SoH 80	no
Cell 04	SoH 80	yes

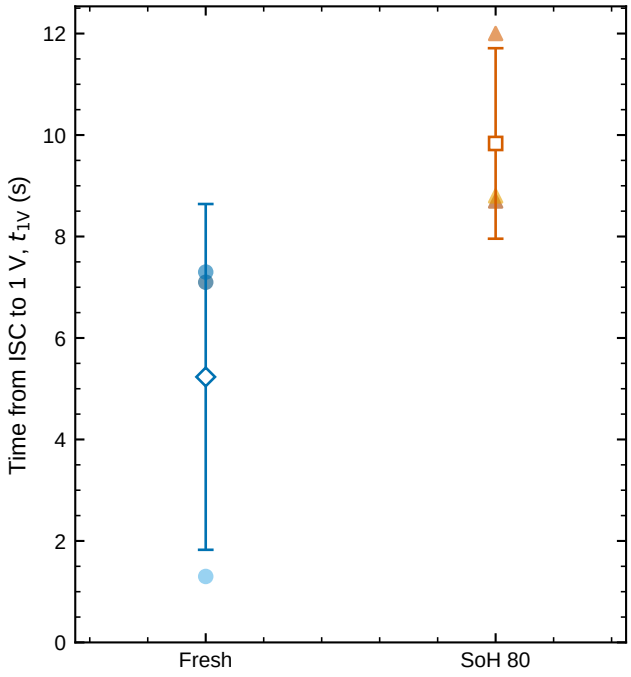

Figure 9. Time from the electrically detected ISC onset to a cell voltage of 1 V. Open symbols show the group mean with standard deviation and filled symbols the individual cells. Marker shape encodes the group in addition to color: circles and open diamonds denote fresh cells, triangles and open squares denote the aged (SoH 80) cells.

In summary, when the aging fixture remained mounted between the first cycle and the abuse test, moderate aging to 80% SoH shifted the initial force buildup and the electrical ISC trigger to smaller intrusion, while the electrical collapse after the trigger became slower and visible gas or aerosol emission was observed less frequently in the aged group.



Figure 10. Post-test condition of the aged cell for which visible gas or aerosol emission was observed (cell 04), shown from two different viewing angles. The local indentation through the opening of the upper plate is visible.

4. Discussion

4.1. Relation to Studies Tested After Release of the Aging Constraint

The pouch-cell studies summarized in Section 1 consistently report characteristic markers shifted to larger intrusion when the cells are indented without external constraint [25–32]. In most of them the cells were aged under compression as well, between screwed flat plates at 0.05 MPa to 0.06 MPa with fixed distance and stronger pressure variations [51] or inside modules, and were released from this constraint before the abuse test, as compiled in [34]. The distinguishing conditions of the present study are therefore the retention of the constraint through the test and its compliant rather than fixed-displacement application. The rightward shift in the force–displacement response is commonly attributed to compliant deposit layers formed on the electrode surfaces during aging, together with gas and irreversible thickness growth [25,27]. The closest counterpart to our experiment is the study of Qu et al., who indented Lithium Cobalt Oxide (LCO)/graphite pouch cells of the same chemistry in the relaxed state after room-temperature cycling to a comparable capacity retention [27]. The cells of the present study shifted in the opposite direction with the aging fixture retained, with the aged cells building up force earlier over most of the pre-peak loading branch and reaching the ISC at 18% smaller displacement. A direct attribution of this contrast to the retained confinement is not possible, since the studies also differ in cell dimensions, aging protocol, and indenter geometry, and a matched group aged under preload and released before the test was not included here. The retained confinement is, however, a physically plausible contributor and one variable that future experiments can control deliberately. A similar correlation between the reported direction of the aging effect and the constraint conditions during aging and testing also emerged from our recent survey of this literature [34]. It is also consistent with the two published exceptions on pouch cells, the large-format automotive cells of Gstrein et al. and the field-aged cells of Abbas et al., in which plating-dominated degradation stiffened the stack and moved the failure to smaller intrusion even without test-side preload [35,36].

Figure 11 illustrates what this rightward shift looks like for an unconstrained pouch cell. In the quasi-static cylindrical indentation of Sprenger et al. (Figure 11a), the force–displacement response of the aged cells is displaced to larger displacement relative to the fresh cells, and the fully charged aged cells reach their force maximum only near 4 mm where the fresh cells have already failed [31]. The cells of the present study, tested with the aging fixture retained, shift the other way.

Mechanistically, the two directions are compatible. Aging generates additional solid material through interphase growth and surface deposits, consumes electrolyte, may generate gas, and expands the electrode stack irreversibly [20,22,51]. Once a cell is released

from its aging constraint, these products end up as free compliant thickness. Pouch slack, gas pockets, and porous deposit layers then act as a soft cushion that the indenter must first compress, which can shift force thresholds to larger displacement [25,27,31]. The results of Liu et al. and Qu et al. show that compression during aging alone does not prevent such deposits from forming [25,27]. The distinguishing condition here is the mechanical state at the start of the test. The unreleased spring load is expected to keep swelling-related thickness, pouch slack, and interfacial gaps partly compressed, which matches the shorter engagement region found in Section 3.3, even if aging-induced deposits are present. Aging may also reduce electrode deformability through coating cracking, binder degradation, and interphase growth [31,35], which could contribute to the earlier ISC beyond the engagement region. Mechanically, the two boundary conditions differ in the free volume available for growing interphase and deposit material. Under a maintained external constraint, this material may be compressed against the confining stack. We hypothesize that this reduces free volume and produces a denser interfacial layer. Stack pressure is known to affect anode porosity and lithium-deposition morphology in graphite-based pouch cells. Wang et al. reported a non-monotonic pressure dependence, with a degradation optimum near 1.25 MPa [51], while Cannarella and Arnold observed increasing surface-film coverage with stack stress [58]. Together, these studies support a pressure-sensitive evolution of the anode surface, but they do not establish deposit compaction or a modulus change at the present preload of 0.11 MPa. The impedance analysis (Section 3.2) is compatible with this picture at the level of magnitude: the polarization arc grew by 67 to 83% while the series resistance grew by 25 to 27%, so the aging-related impedance change is carried mainly by processes at the electrode–electrolyte interfaces rather than by the ohmic path. The two-electrode measurement does not permit this increase to be assigned to a specific interfacial process, and a larger polarization resistance is not by itself evidence of interphase growth. A related confinement effect may also play a role in the earlier or unchanged onsets reported for hard-cased cylindrical cells, whose casing maintains the constraint throughout life by construction [30,37–39], although differences in geometry and failure mode prevent a direct transfer.

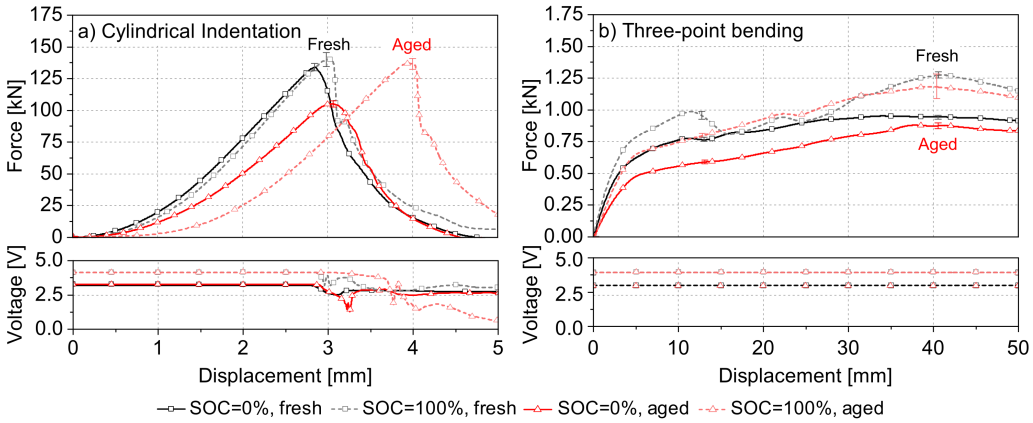

Figure 11. Force–displacement (**top**) and voltage (**bottom**) response of fresh and electrically aged (SoH 90%) Nickel Manganese Cobalt Oxide (NMC) pouch cells under (**a**) quasi-static cylindrical indentation and (**b**) three-point bending at 0% and 100% SoC, tested without external constraint. Panel (**a**) shows the rightward shift of the aged force–displacement curves that is characteristic of unconstrained pouch-cell studies and opposite to the response observed here with the aging fixture retained; the comparison is illustrative and not a matched experiment. Reproduced from Sprenger et al. [31], *Energies* **2022**, *15*, 847, published by MDPI under the Creative Commons CC BY 4.0 license.

The lower scatter of the aged group across most mechanical descriptors fits this picture as well. The fresh cells, which were installed in the fixture only minutes before the test, scatter more widely along the loading branch, whereas the aged cells, mechanically conditioned by several months in the fixture, respond more uniformly. With three cells per group this comparison remains exploratory.

4.2. Earlier Trigger, Slower Electrical Collapse

The aged cells short-circuited earlier, but their voltage collapsed more slowly, with the time from ISC onset to 1 V nearly doubling. Visible gas or aerosol emission was observed in all three fresh-cell tests and in one of the three aged-cell tests. This decoupling of trigger position and subsequent electrical and visual response resembles patterns reported for unconstrained aged pouch cells [25,27,28,33] and for aged cylindrical cells [39,40]. The outcome depends on the aging mechanism, however; lithium-plating-dominated cells can exhibit more severe thermal responses than fresh ones [36,41,42]. The lower available charge may contribute to the slower voltage collapse. The impedance measurements independently characterize the aged state, but a direct causal link between the spectral changes and the mechanical or post-trigger response cannot be established from the present measurements. The actual short-path resistance, short-circuit current, and heat-release rate were not measured. For safety assessment, trigger position and post-trigger behavior must therefore be considered separately. Whether the longer electrical interval provides usable time for detection or mitigation was not investigated, and the qualitative visual observations should not be interpreted as evidence of a less severe thermal response.

4.3. Limitations

The scope of this study was deliberately narrow and focused on the response obtained when the aging fixture remains mounted through the abuse test. Several limitations remain. First, the sample size of three cells per group permits only descriptive statistics. The fresh group in particular scatters more widely along the loading branch, which limits the precision of the fresh-group means, although the direction of the onset metrics, from the reference-force displacements to the ISC onset, was consistent across all three cells. The non-overlapping ranges for selected displacement descriptors describe a consistent ordering within the six tested cells but do not establish a population-level effect. Independent confirmation with a larger sample is required. Second, a single preload of 0.11 MPa was examined. This value is representative of initial module compressions, but recent degradation studies operate at pressures up to 1 MPa [45,51], and both the aging pathway and the abuse response may depend nonlinearly on pressure, so the observed magnitudes cannot be extrapolated beyond the investigated value. Third, one aging path (room-temperature 1C full cycles), one terminal SoH of about 80%, and one test SoC of 100% were covered, whereas the aging path is known to influence the mechanical response at least as strongly as the aging depth [31,35,39]. Fourth, the preload was set and verified at installation but not logged continuously, so the redistribution of the spring load through reversible breathing and irreversible growth over life is not quantified [46,50]. Fifth, no group aged under preload and released before the abuse test was included, and no uncycled cells were stored under preload for the duration of the campaign, so neither the causal role of the unreleased confinement nor the contribution of long-term mechanical conditioning can be separated from cycling-induced aging within this dataset. Sixth, the response after the trigger was assessed electrically and through qualitative review of the test recordings and post-test condition. The groups were matched by nominal SoC rather than by absolute charge, so the post-trigger comparison combines aging-related changes with the lower stored charge of the aged cells. Seventh, only one cathode chemistry, LCO

paired with a graphite anode, was examined. The proposed mechanism involves interphase and deposit growth at the graphite anode and its mechanical engagement with the separator under sustained constraint. Because mechanically initiated internal short circuits depend on separator integrity and electrode contact area [59], this pathway may also be relevant to other graphite-based chemistries. Cathode chemistry can nevertheless alter the aging path through effects such as swelling and gas generation. The experimental finding therefore remains specific to the tested LCO/graphite cells. Eighth, all abuse tests were conducted at a single quasi-static displacement rate of 0.125 mm s^{-1}. Strain-rate sensitivity is well established for fresh Lithium-Ion pouch cells [10,60]. Studies combining electrochemical aging with different loading rates indicate that aging-related displacement shifts can persist at higher rates, while their magnitude and the corresponding force response depend on loading rate and SoC [32,33]. Neither study used a retained aging constraint. Whether the earlier engagement and ISC onset observed here persist under dynamic loading in the present constrained configuration therefore remains undetermined. Finally, no component-level post-mortem analysis by disassembly, microscopy, or computed tomography was performed, so the mechanism proposed in Section 4.1 is inferred from macroscopic observables. Direct microstructural assessment would require separate cells sampled after constrained aging and before mechanical abuse. All cells in the present campaign underwent indentation to structural collapse and ISC, so their post-test surfaces combine aging- and abuse-related changes. In a comparable graphite/NMC pouch-cell system, Scanning Electron Microscopy (SEM)-EDX showed a fluorine- and phosphorus-rich anode surface layer, anode thickening, and morphological indications of local lithium plating [32]. Because SEM-EDX does not detect lithium directly, the plating interpretation in that study relies on morphology and accompanying decomposition products. A dedicated post-mortem campaign using established disassembly and characterization methods [61] should examine cells after aging under retained constraint and before abuse to distinguish deposit compaction from plating-dominated stiffening.

4.4. Perspectives

The next experimental step should separate the contributions that are combined in the present comparison. A matched group aged under preload and released before the abuse test would isolate the effect of constraint continuity, while uncycled cells held under preload for the same duration would distinguish long-term mechanical conditioning from cycling-induced aging. The sample size should be determined prospectively using the present observations as pilot information, a pre-defined minimum effect of practical relevance, and conservative variance assumptions. Post-mortem analysis of cells sampled after constrained aging and before abuse should then distinguish deposit compaction from plating-dominated stiffening. Additional preload levels, SoH stages, and test SoC values would then establish whether the observed shift varies systematically with pressure, aging depth, and reversible swelling [46,50,53].

Continuous preload logging, periodic thickness or pressure-distribution measurements, integrated surface-temperature sensing, and post-mortem analysis would connect the evolving boundary condition to the failure mechanism. Dynamic loading [10,39] and fixed-displacement fixtures [50] would extend the findings toward additional module conditions. Fresh-to-aged abuse comparisons on pouch cells should report the preload magnitude, fixture stiffness, pressure evolution or its absence, and whether the aging constraint was released before testing [6].

5. Conclusions

In this study, pouch cells were aged and mechanically abused without removing or readjusting a preload fixture initialized at a nominal average stack pressure of 0.11 MPa. Commercial 6 Ah pouch cells were cycled to approximately 80% SoH in this fixture and subsequently indented quasi-statically at nominally 100% SoC; uncycled references were tested in the corresponding reused fixture configuration after inspection and re-establishment of the nominal initial preload. The principal findings are as follows.

First, the aged cells built up force at smaller intrusion. They reached 20 kN at 11% smaller displacement, and the electrically detected ISC onset occurred at 18% smaller displacement and at a 10% lower group-mean force. The intrusion interval from 10 kN to ISC onset was also 19% shorter, showing that the earlier trigger was not solely an offset of the initial toe region. Its direction was unchanged across voltage-drop thresholds of 50 mV to 200 mV. By contrast, the global peak and work-to-peak descriptors showed no clear group-level shift within the observed cell-to-cell scatter. The direction of this response differs from many pouch-cell studies in which the aging constraint was released before testing and is consistent with confinement history being a contributing boundary condition; the present design does not isolate it as the sole cause.

Second, following the electrically detected ISC onset, the time to a cell voltage of 1 V increased from 5.2 ± 3.4 to 9.8 ± 1.9 s in the aged group. This interval is used as a secondary descriptor of voltage decay. Assessment of thermal severity would require measurements of short-circuit current, short-path resistance, and heat release together with control of absolute charge. Visible gas or aerosol emission was observed in all three fresh-cell tests and in one of the three aged-cell tests and is reported as a qualitative observation.

The experiments show a consistent directional response within the six tested cells under maintained confinement, identifying confinement continuity as a relevant boundary condition. A matched group released after aging is required to isolate its causal contribution. Confirmation at population level and transfer to other cell formats, chemistries, fixture stiffnesses, pressures, and dynamic loading conditions require dedicated studies. Fresh-to-aged abuse comparisons on pouch cells should report the nominal preload, fixture stiffness, pressure-evolution measurement or its absence, and whether the aging constraint was released before testing.

Supplementary Materials: The following supporting information can be downloaded at: https://www.mdpi.com/article/10.3390/batteries12090361/, Data S1 (XLSX): processed per-cell reference-capacity, impedance and quasi-static indentation characteristic values, including the internal short-circuit trigger threshold-sensitivity results; the individual-cell values underlying Table 1 and the statistical and equivalent-circuit analyses reported in the article.

Author Contributions: Conceptualization, R.P.; methodology, R.P.; software, R.P. and V.T.; validation, R.P. and V.T.; formal analysis, R.P.; investigation, R.P.; resources, H.-G.S.; data curation, R.P.; writing—original draft preparation, R.P.; writing—review and editing, R.P., V.T., S.D. and H.-G.S.; visualization, R.P.; supervision, S.D. and H.-G.S.; project administration, R.P. All authors have read and agreed to the published version of the manuscript.

Funding: The research itself received no external project funding. The article processing charge was funded by the Open Access Publication Fund of Technische Hochschule Ingolstadt (THI) and by the Federal Ministry of Research, Technology and Space (BMFTR) through the FH-Personal project PTT_THI (grant number 03FHP188).

Data Availability Statement: Processed per-cell capacity, impedance, indentation, and short-circuit threshold-sensitivity data supporting the reported results are provided in Supplementary Data S1, together with the statistical and equivalent-circuit analyses reported here.

Acknowledgments: During the preparation of this work, the authors used Grammarly for Microsoft Edge (version 14.1134.0) and ChatGPT using GPT-5.5 and GPT-5.6 Thinking (OpenAI) solely for language editing and improvements in readability. The authors reviewed and edited all outputs as needed and take full responsibility for the content of the publication.

Conflicts of Interest: The authors declare no conflicts of interest.

Abbreviations

The following abbreviations are used in this manuscript:

BoL	Beginning of Life
CC-CV	Constant Current–Constant Voltage
DoD	Depth of Discharge
EIS	Electrochemical Impedance Spectroscopy
ISC	Internal Short Circuit
LIB	Lithium-Ion Battery
LIBs	Lithium-Ion Batteries
SEM	Scanning Electron Microscopy
NMC	Nickel Manganese Cobalt Oxide
LCO	Lithium Cobalt Oxide
LFP	Lithium Iron Phosphate
SoC	State of Charge
SoH	State of Health
TR	Thermal Runaway

References

1. Schmuch, R.; Wagner, R.; Hörpel, G.; Placke, T.; Winter, M. Performance and cost of materials for lithium-based rechargeable automotive batteries. *Nat. Energy* **2018**, *3*, 267–278. https://doi.org/10.1038/s41560-018-0107-2.
2. Kukreja, J.; Nguyen, T.; Siegmund, T.; Chen, W.; Tsutsui, W.; Balakrishnan, K.; Liao, H.; Parab, N. Crash analysis of a conceptual electric vehicle with a damage tolerant battery pack. *Extrem. Mech. Lett.* **2016**, *9*, 371–378. https://doi.org/10.1016/j.eml.2016.05.004.
3. Wang, H.; Simunovic, S.; Maleki, H.; Howard, J.N.; Hallmark, J.A. Internal configuration of prismatic lithium-ion cells at the onset of mechanically induced short circuit. *J. Power Sources* **2016**, *306*, 424–430. https://doi.org/10.1016/j.jpowsour.2015.12.026.
4. Feng, X.; Fang, M.; He, X.; Ouyang, M.; Lu, L.; Wang, H.; Zhang, M. Thermal runaway features of large format prismatic lithium ion battery using extended volume accelerating rate calorimetry. *J. Power Sources* **2014**, *255*, 294–301. https://doi.org/10.1016/j.jpowsour.2014.01.005.
5. Luo, H.; Jiang, X.; Xia, Y.; Zhou, Q. Fracture Mode Analysis of Lithium-Ion Battery Under Mechanical Loading. In *Proceedings of the ASME International Mechanical Engineering Congress and Exposition, Houston, TX, USA, 13–19 November 2015*; ASME: New York, NY, USA, 2016. https://doi.org/10.1115/IMECE2015-52595.
6. Ruiz, V.; Pfrang, A.; Kriston, A.; Omar, N.; van den Bossche, P.; Boon-Brett, L. A review of international abuse testing standards and regulations for lithium ion batteries in electric and hybrid electric vehicles. *Renew. Sustain. Energy Rev.* **2018**, *81*, 1427–1452. https://doi.org/10.1016/j.rser.2017.05.195.
7. Kotak, B.; Kotak, Y.; Brade, K.; Kubjatko, T.; Schweiger, H.G. Battery Crush Test Procedures in Standards and Regulation: Need for Augmentation and Harmonisation. *Batteries* **2021**, *7*, 63. https://doi.org/10.3390/batteries7030063.
8. Sahraei, E.; Meier, J.; Wierzbicki, T. Characterizing and modeling mechanical properties and onset of short circuit for three types of lithium-ion pouch cells. *J. Power Sources* **2014**, *247*, 503–516. https://doi.org/10.1016/j.jpowsour.2013.08.056.
9. Greve, L.; Fehrenbach, C. Mechanical testing and macro-mechanical finite element simulation of the deformation, fracture, and short circuit initiation of cylindrical Lithium ion battery cells. *J. Power Sources* **2012**, *214*, 377–385. https://doi.org/10.1016/j.jpowsour.2012.04.055.
10. Kisters, T.; Sahraei, E.; Wierzbicki, T. Dynamic impact tests on lithium-ion cells. *Int. J. Impact Eng.* **2017**, *108*, 205–216. https://doi.org/10.1016/j.ijimpeng.2017.04.025.
11. Kotter, P.; Kisters, T.; Schleicher, A. Dynamic impact tests to characterize the crashworthiness of large-format lithium-ion cells. *J. Energy Storage* **2019**, *26*, 100948. https://doi.org/10.1016/j.est.2019.100948.
12. Chung, S.H.; Tancogne-Dejean, T.; Zhu, J.; Luo, H.; Wierzbicki, T. Failure in lithium-ion batteries under transverse indentation loading. *J. Power Sources* **2018**, *389*, 148–159. https://doi.org/10.1016/j.jpowsour.2018.04.003.

13. Xu, J.; Liu, B.; Wang, X.; Hu, D. Computational model of 18650 lithium-ion battery with coupled strain rate and SOC dependencies. *Appl. Energy* **2016**, *172*, 180–189. https://doi.org/10.1016/j.apenergy.2016.03.108.
14. Dixon, B.; Mason, A.; Sahraei, E. Effects of electrolyte, loading rate and location of indentation on mechanical integrity of li-ion pouch cells. *J. Power Sources* **2018**, *396*, 412–420. https://doi.org/10.1016/j.jpowsour.2018.06.042.
15. Fasching, M.; Grollitsch, S.; Höschele, P.; Schmid, A.; Ellersdorfer, C. Investigating the mechanical in-plane characteristics of lithium-ion pouch cells under crush loads. *J. Energy Storage* **2024**, *89*, 111581. https://doi.org/10.1016/j.est.2024.111581.
16. Deng, J.; Smith, I.; Bae, C.; Rairigh, P.; Miller, T.; Surampudi, B.; L'Eplattenier, P.; Caldichoury, I. Impact Modeling and Testing of Pouch and Prismatic Cells. *J. Electrochem. Soc.* **2020**, *167*, 090550. https://doi.org/10.1149/1945-7111/ab9962.
17. Zhu, J.; Wierzbicki, T.; Li, W. A review of safety-focused mechanical modeling of commercial lithium-ion batteries. *J. Power Sources* **2018**, *378*, 153–168. https://doi.org/10.1016/j.jpowsour.2017.12.034.
18. Song, Y.; Bulla, M.; Patanwala, H.; Sahraei, E. Validation of Sahraei Failure Criterion on cylindrical and pouch Lithium-ion battery cells. *J. Energy Storage* **2024**, *94*, 112371. https://doi.org/10.1016/j.est.2024.112371.
19. Zhu, J. Standardizing mechanical tests on li-ion batteries to develop a useful cell-level model under extreme mechanical loads. *J. Energy Storage* **2023**, *65*, 107320. https://doi.org/10.1016/j.est.2023.107320.
20. Edge, J.S.; O'Kane, S.; Prosser, R.; Kirkaldy, N.D.; Patel, A.N.; Hales, A.; Ghosh, A.; Ai, W.; Chen, J.; Yang, J.; et al. Lithium ion battery degradation: What you need to know. *Phys. Chem. Chem. Phys. PCCP* **2021**, *23*, 8200–8221. https://doi.org/10.1039/d1cp00359c.
21. Ecker, M.; Shafiei Sabet, P.; Sauer, D.U. Influence of operational condition on lithium plating for commercial lithium-ion batteries—Electrochemical experiments and post-mortem-analysis. *Appl. Energy* **2017**, *206*, 934–946. https://doi.org/10.1016/j.apenergy.2017.08.034.
22. Zhang, X.; Zhu, J.; Sahraei, E. Degradation of battery separators under charge–discharge cycles. *RSC Adv.* **2017**, *7*, 56099–56107. https://doi.org/10.1039/C7RA11585G.
23. von Lüders, C.; Zinth, V.; Erhard, S.V.; Osswald, P.J.; Hofmann, M.; Gilles, R.; Jossen, A. Lithium plating in lithium-ion batteries investigated by voltage relaxation and in situ neutron diffraction. *J. Power Sources* **2017**, *342*, 17–23. https://doi.org/10.1016/j.jpowsour.2016.12.032.
24. Hartmann, L.; Reuter, L.; Wallisch, L.; Beiersdorfer, A.; Adam, A.; Goldbach, D.; Teufl, T.; Lamp, P.; Gasteiger, H.A.; Wandt, J. Depletion of Electrolyte Salt Upon Calendaric Aging of Lithium-Ion Batteries and its Effect on Cell Performance. *J. Electrochem. Soc.* **2024**, *171*, 060506. https://doi.org/10.1149/1945-7111/ad4821.
25. Liu, Y.; Xia, Y.; Zhou, Q. Effect of low-temperature aging on the safety performance of lithium-ion pouch cells under mechanical abuse condition: A comprehensive experimental investigation. *Energy Storage Mater.* **2021**, *40*, 268–281. https://doi.org/10.1016/j.ensm.2021.05.022.
26. Kovachev, G.; Ellersdorfer, C.; Gstrein, G.; Hanzu, I.; Wilkening, H.M.R.; Werling, T.; Schauwecker, F.; Sinz, W. Safety assessment of electrically cycled cells at high temperatures under mechanical crush loads. *eTransportation* **2020**, *6*, 100087. https://doi.org/10.1016/j.etran.2020.100087.
27. Qu, Y.; Xing, B.; Xia, Y.; Zhou, Q. How does room temperature cycling ageing affect lithium-ion battery behaviors under extreme indentation? *eTransportation* **2024**, *20*, 100331. https://doi.org/10.1016/j.etran.2024.100331.
28. Jia, Y.; Gao, X.; Ma, L.; Xu, J. Comprehensive Battery Safety Risk Evaluation: Aged Cells versus Fresh Cells Upon Mechanical Abusive Loadings. *Adv. Energy Mater.* **2023**, *13*, 2300368. https://doi.org/10.1002/aenm.202300368.
29. Guo, Z.; Ma, Z.; Liu, J.; Zhao, W.; Wang, S.; Zhao, H.; Ren, L. Overcharging cycle aging-induced severe degradation of safety properties of lithium-ion pouch battery cells subjected to mechanical abuse. *Energy* **2025**, *320*, 135168. https://doi.org/10.1016/j.energy.2025.135168.
30. Spettmann, C.; Shin, J.; Qu, Y.; Liu, Y.; Xia, Y. Low-Temperature Aging Effect on Safety of Lithium-Ion Batteries Subjected to Intrusion: A Comparative Study of 18650 and Pouch Cells. In *Proceedings of the WCX SAE World Congress Experience, Detroit, MI, USA, 16–18 April 2024*; SAE Technical Paper Series; Spettmann, C.; Shin, J.; Qu, Y.; Liu, Y.; Xia, Y., Eds.; SAE International: Warrendale, PA, USA, 2024. https://doi.org/10.4271/2024-01-2063.
31. Sprenger, M.; Dölle, N.; Schauwecker, F.; Raffler, M.; Ellersdorfer, C.; Sinz, W. Multiscale Analysis and Safety Assessment of Fresh and Electrical Aged Lithium-Ion Pouch Cells Focusing on Mechanical Behavior. *Energies* **2022**, *15*, 847. https://doi.org/10.3390/en15030847.
32. Sprenger, M.; Kovachev, G.; Dölle, N.; Schauwecker, F.; Sinz, W.; Ellersdorfer, C. Changes in the Mechanical Behavior of Electrically Aged Lithium-Ion Pouch Cells: In-Plane and Out-of-Plane Indentation Loads with Varying Testing Velocity and State of Charge. *Batteries* **2023**, *9*, 67. https://doi.org/10.3390/batteries9020067.
33. Liu, Y.; Xia, Y.; Xing, B.; Zhou, Q. Mechanical-electrical-thermal responses of lithium-ion pouch cells under dynamic loading: A comparative study between fresh cells and aged ones. *Int. J. Impact Eng.* **2022**, *166*, 104237. https://doi.org/10.1016/j.ijimpeng.2022.104237.

34. Polzer, R.; Rufino Júnior, C.A.; Diel, S.; Schweiger, H.G. Mechanical Intrusion of Aged Lithium-Ion Batteries: Boundary-Condition Continuity, Trigger Definitions, and the Limits of Cross-Study Comparability. *Batteries* **2026**, *12*, 282. https://doi.org/10.3390/batteries12080282.
35. Gstrein, G.; Abbas, S.M.; Ewert, E.; Wenzl, M.; Ellersdorfer, C. Safety-Critical Influence of Ageing on Mechanical Properties of Lithium-Ion Pouch Cells. *Batteries* **2025**, *11*, 99. https://doi.org/10.3390/batteries11030099.
36. Abbas, S.M.; Gstrein, G.; Jauernig, A.D.; Schmid, A.; Michelini, E.; Hinterberger, M.; Ellersdorfer, C. Influence of Lithium Plating on the Mechanical Properties of Automotive High-Energy Pouch Batteries. *Batteries* **2025**, *11*, 330. https://doi.org/10.3390/batteries11090330.
37. Friesen, A.; Horsthemke, F.; Mönnighoff, X.; Brunklaus, G.; Krafft, R.; Börner, M.; Risthaus, T.; Winter, M.; Schappacher, F.M. Impact of cycling at low temperatures on the safety behavior of 18650-type lithium ion cells: Combined study of mechanical and thermal abuse testing accompanied by post-mortem analysis. *J. Power Sources* **2016**, *334*, 1–11. https://doi.org/10.1016/j.jpowsour.2016.09.120.
38. Xu, J.; Jia, Y.; Liu, B.; Zhao, H.; Yu, H.; Li, J.; Yin, S. Coupling Effect of State-of-Health and State-of-Charge on the Mechanical Integrity of Lithium-Ion Batteries. *Exp. Mech.* **2018**, *58*, 633–643. https://doi.org/10.1007/s11340-018-0380-9.
39. Polzer, R.; Heider, E.; Ellersdorfer, C.; Golla-Schindler, U.; Rufino Júnior, C.A.; Diel, S.; Schweiger, H.G. Effect of Electrochemical Aging on the Mechanical–Electrical–Thermal Safety Response of Tabless 4695 Cylindrical Cells Under Quasi-Static Indentation. *Batteries* **2026**, *12*, 179. https://doi.org/10.3390/batteries12050179.
40. Preger, Y.; Feinauer, M.; Torres-Castro, L.; Hogrefe, C.; Gray, L.; Gerosa, G.; Langendorf, J.; Häfele, S.; Wittman, R.M.; Wörz, M.; et al. Impact of Testing Method on Safety Assessment of Aged Li-Ion Cells: Part II—Aged Cells Without Li Plating. *J. Electrochem. Soc.* **2025**, *172*, 080503. https://doi.org/10.1149/1945-7111/adeed0.
41. Gerosa, G.G.; Feinauer, M.; Hogrefe, C.; Häfele, S.; Bischof, K.; Wörz, M.; Böse, O.; Wohlfahrt-Mehrens, M.; Hölzle, M.; Waldmann, T. Impact of Testing Method on Safety Assessment of Aged Li-ion Cells: Part I—Li Plating as Main Aging Mechanism. *J. Electrochem. Soc.* **2025**, *172*, 030502. https://doi.org/10.1149/1945-7111/adb804.
42. Feinauer, M.; Abd-El-Latif, A.A.; Sichler, P.; Wohlfahrt-Mehrens, M.; Hölzle, M.; Waldmann, T. Effects of Main Aging Mechanism and State of Charge on the Safety of 21700 Li-Ion Battery Cells with Ni-Rich NMC Cathode. *J. Electrochem. Soc.* **2024**, *171*, 110524. https://doi.org/10.1149/1945-7111/ad9356.
43. Cannarella, J.; Arnold, C.B. State of health and charge measurements in lithium-ion batteries using mechanical stress. *J. Power Sources* **2014**, *269*, 7–14. https://doi.org/10.1016/j.jpowsour.2014.07.003.
44. Madani, S.S.; Schaltz, E.; Kær, S.K. Characterization of the Compressive Load on a Lithium-Ion Battery for Electric Vehicle Application. *Machines* **2021**, *9*, 71. https://doi.org/10.3390/machines9040071.
45. Aufschläger, A.; Durdel, A.; Kraft, L.; Jossen, A. Optimizing mechanical compression for cycle life and irreversible swelling of high energy and high power lithium-ion pouch cells. *J. Energy Storage* **2024**, *76*, 109883. https://doi.org/10.1016/j.est.2023.109883.
46. Höschele, P.; Heindl, S.F.; Erker, S.; Ellersdorfer, C. Influence of reversible swelling and preload force on the failure behavior of a lithium-ion pouch cell tested under realistic boundary conditions. *J. Energy Storage* **2023**, *65*, 107228. https://doi.org/10.1016/j.est.2023.107228.
47. Mussa, A.S.; Lindbergh, G.; Klett, M.; Gudmundson, P.; Svens, P.; Lindström, R.W. Inhomogeneous active layer contact loss in a cycled prismatic lithium-ion cell caused by the jelly-roll curvature. *J. Energy Storage* **2018**, *20*, 213–217. https://doi.org/10.1016/j.est.2018.09.012.
48. Xiong, R.; Li, H.; Mei, B.A.; He, H.; Shen, W. Revealing the effect of external pressure on solid-electrolyte interphase and lithium plating in lithium-ion batteries. *J. Energy Chem.* **2025**, *102*, 734–744. https://doi.org/10.1016/j.jechem.2024.11.021.
49. Preimesberger, J.I.; Chen, Y.; An, K.; Arnold, C.B. Understanding the effect of cycling lithium-ion pouch cells under stress using neutron diffraction. *J. Power Sources* **2024**, *598*, 234114. https://doi.org/10.1016/j.jpowsour.2024.234114.
50. Schommer, A.; Orozco Corzo, M.; Henshall, P.; Morrey, D.; Collier, G. Stack pressure on lithium-ion pouch cells: A comparative study of constant pressure and fixed displacement devices. *J. Power Sources* **2025**, *629*, 236019. https://doi.org/10.1016/j.jpowsour.2024.236019.
51. Wang, H.; Wang, R.; O'Keefe, C.A.; Björklund, E.; Proprentner, D.; Stallard, J.C.; Tan, H.J.; Dose, W.M.; Piper, L.F.J.; Weatherup, R.S.; et al. The interplay between stack pressure, mechanical expansion and degradation pathways in lithium-ion batteries. *Nat. Energy* **2026**, *11*, 1032–1042. https://doi.org/10.1038/s41560-026-02087-6.
52. Hahn, A.; Doose, S.; Saathoff, D.; Kwade, A. Effect of External Compression on the Thermal Runaway of Lithium-Ion Battery Cells during Crush Tests: Insights for Improved Safety Assessment. *Batteries* **2023**, *9*, 404. https://doi.org/10.3390/batteries9080404.
53. Höschele, P.; Ellersdorfer, C. Implementing Reversible Swelling into the Numerical Model of a Lithium-Ion Pouch Cell for Short Circuit Prediction. *Batteries* **2023**, *9*, 417. https://doi.org/10.3390/batteries9080417.
54. Schönleber, M.; Klotz, D.; Ivers-Tiffée, E. A Method for Improving the Robustness of linear Kramers-Kronig Validity Tests. *Electrochim. Acta* **2014**, *131*, 20–27. https://doi.org/10.1016/j.electacta.2014.01.034.

55. Lamb, J.; Orendorff, C.J. Evaluation of mechanical abuse techniques in lithium ion batteries. *J. Power Sources* **2014**, *247*, 189–196. https://doi.org/10.1016/j.jpowsour.2013.08.066.
56. Cohen, J. *Statistical Power Analysis for the Behavioral Sciences*, 2nd ed.; Lawrence Erlbaum Associates: Hillsdale, NJ, USA, 1988.
57. Hedges, L.V. Distribution Theory for Glass's Estimator of Effect Size and Related Estimators. *J. Educ. Stat.* **1981**, *6*, 107–128. https://doi.org/10.3102/10769986006002107.
58. Cannarella, J.; Arnold, C.B. Stress evolution and capacity fade in constrained lithium-ion pouch cells. *J. Power Sources* **2014**, *245*, 745–751. https://doi.org/10.1016/j.jpowsour.2013.06.165.
59. Zhang, X.; Sahraei, E.; Wang, K. Li-ion Battery Separators, Mechanical Integrity and Failure Mechanisms Leading to Soft and Hard Internal Shorts. *Sci. Rep.* **2016**, *6*, 32578. https://doi.org/10.1038/srep32578.
60. Akbari, E.; Voyiadjis, G.Z. Stress and Strain Characterization for Evaluating Mechanical Safety of Lithium-Ion Pouch Batteries under Static and Dynamic Loadings. *Batteries* **2024**, *10*, 309. https://doi.org/10.3390/batteries10090309.
61. Waldmann, T.; Iturrondobeitia, A.; Kasper, M.; Ghanbari, N.; Aguesse, F.; Bekaert, E.; Daniel, L.; Genies, S.; Gordon, I.J.; Löble, M.W.; et al. Review—Post-Mortem Analysis of Aged Lithium-Ion Batteries: Disassembly Methodology and Physico-Chemical Analysis Techniques. *J. Electrochem. Soc.* **2016**, *163*, A2149–A2164. https://doi.org/10.1149/2.1211609jes.

Disclaimer/Publisher's Note: The statements, opinions and data contained in all publications are solely those of the individual author(s) and contributor(s) and not of MDPI and/or the editor(s). MDPI and/or the editor(s) disclaim responsibility for any injury to people or property resulting from any ideas, methods, instructions or products referred to in the content.